Numerical simulation of shock propagation in a polydisperse bubbly liquid

Keita Ando *, Tim Colonius, Christopher E. Brennen

Division of Engineering and Applied Science, California Institute of Technology, Pasadena, CA 91125, United States

ARTICLE INFO

ABSTRACT

The effect of distributed bubble nuclei sizes on shock propagation in a bubbly liquid is numerically investigated. An ensemble-averaged technique is employed to derive the statistically averaged conservation laws for polydisperse bubbly flows. A finite-volume method is developed to solve the continuum bubbly flow equations coupled to a single-bubble-dynamic equation that incorporates the effects of heat transfer, liquid viscosity and compressibility. The one-dimensional shock computations reveal that the distribution of equilibrium bubble sizes leads to an apparent damping of the averaged shock dynamics due to phase cancellations in oscillations of the different-sized bubbles. If the distribution is sufficiently broad, the phase cancellation effect can dominate over the single-bubble-dynamic dissipation and the averaged shock profile is smoothed out.

1. Introduction

Complex bubbly flows are ubiquitous in engineering flows, such as underwater explosions, industrial piping systems and hydraulic machinery (Cole, 1948; Wylie and Streeter, 1993; Brennen, 1994). Seawater near the sea surface contains fairly big bubbles due to breaking waves. Even for liquid flows with small nuclei populations, the interaction with structures often produces tension waves that can cause cavitation, and complex two-phase flow regimes are encountered. The resulting gas or vapor bubbles lead to wave dispersion; the dynamics of bubbly mixtures cannot be properly described by simple barotropic relations (Brennen, 1995, 2005). An understanding of complex dynamics of such bubbly flows is still inadequate for many engineering applications.

Theoretical and numerical models have been developed to investigate shock dynamics in bubbly flows. In the classic papers of van Wijngaarden (1968, 1972), volume-averaged mixture quantities were defined in order to average out local scattering due to the dynamics of individual bubbles, and averaged conservation laws for bubbly flows were formulated based on heuristic reasoning. Zhang and Prosperetti (1994) developed an ensemble-averaging technique to derive the mixture-averaged equations. The computations of the mixture-averaged equations coupled to a Rayleigh–Plesset-type equation for single bubble dynamics (Nigmatulin et al.,

1988; Watanabe and Prosperetti, 1994; Kameda and Matsumoto, 1996; Kameda et al., 1998) reproduced averaged shock structures. The direct numerical simulations of shock propagation in bubbly liquids (Delale et al., 2005; Delale and Tryggvason, 2008; Seo et al., 2010) are an important step to quantify the effect of direct interactions between the neighboring bubbles.

A finite cloud of bubbles has been extensively studied as a canonical example. One of the earliest attempts is the work of van Wijngaarden (1964) that considered the collapse of a bubbly layer near a wall. The study of the linearized dynamics of spherical bubble clouds (d'Agostino and Brennen, 1989) identified the natural frequencies of the cloud that can be much smaller than the natural frequency of individual bubble oscillations. The nonlinear computations of bubble clouds (Chahine, 1982; Omta, 1987; Wang and Brennen, 1999; Colonius et al., 2000) indicate that cloud collapse can generate higher pressure than that predicted by superposition of single-bubble calculations in the corresponding one-way-coupling case (in which interactions among the bubbles through the averaged field are ignored); this violent cloud collapse may account for cavitation noise and erosion. All of the above analyses were confined to the case of monodisperse mixtures. However, the computations of a spherical bubble cloud with a distribution of equilibrium bubble sizes (Wang, 1999; Shimada et al., 2000) suggest a profound impact of polydispersity on the averaged dynamics.

The continuum models have been validated by experiments. In the pioneering work of Campbell and Pitcher (1958), shock propagation in a bubbly liquid-filled, vertical tube was considered, and their results showed reasonable agreement with the steady shock relations derived from mixture-averaged equations. Subsequent experiments (Noordzij and van Wijngaarden, 1974; Beylich and

* Corresponding author. Present address: School of Electrical and Electronic Engineering, Nanyang Technological University, Singapore 639798, Singapore. Tel.: +65 6790 6534.
E-mail addresses: kando@ntu.edu.sg (K. Ando), colonius@caltech.edu (T. Colonius), brennen@caltech.edu (C.E. Brennen).

Gülhan, 1990; Kameda and Matsumoto, 1996; Kameda et al., 1998) used a similar device with careful control of bubble sizes, and identified oscillatory shock structures. Beylich and Gülhan (1990) reported on the polydisperse case in which the smoothed shock structure was seen. Unfortunately, experimental observations on the shock dynamics of polydisperse mixtures are rather limited.

The goals of this paper are to derive a continuum bubbly flow model that incorporates a distribution of equilibrium bubble nuclei sizes and quantify the effect of polydispersity on averaged shock dynamics. In Section 2, the continuum and single-bubble-dynamic models with their limitations are presented. One-way-coupled flow computations are also considered in order to clarify some fundamental issues arising in polydisperse flows. Section 3 provides the numerical implementation and its verification with linear problems. In Section 4, one-dimensional shock propagation through a bubbly liquid and a bubble screen is computed, and the effect of polydispersity on the averaged shock dynamics is investigated. Finally, we summarize the findings in Section 5.

2. Physical model

2.1. Continuum bubbly flow model

2.1.1. Ensemble-averaged equations

With the ensemble-averaging technique of Zhang and Prosperetti (1994), one may formally derive continuum models in order to evaluate the average mixture dynamics. The key concept is to statistically treat the dynamical state of bubbly mixtures in which a large number of realizations of spherical bubbles (or isotropic scatters) exist. In other words, we discard any scattering effects in a specific realization, but explore the statistically averaged dynamics. Even though direct interactions between the neighboring bubbles are minimal, there can still appear indirect interactions among the bubbles through the averaged field; the problem is *two-way-coupled*. In what follows, we present the ensemble-averaged conservation laws for polydisperse bubbly flows with the model assumptions. The complete derivation can be found in Zhang and Prosperetti (1994) and is also summarized in Ando (2010).

The continuum model assumes that (a) the bubbles are spherical; (b) mutual interactions among the bubbles are negligible except through their effect on the mixture-averaged flow; (c) wavelengths in the mixture are large compared to the mean bubble spacing; (d) the bubbles advect with the ambient liquid velocity; and (e) density and velocity fluctuations in the liquid phase are uncorrelated.

Assumption (a) implies that fission and coalescence of the bubbles are not permitted, so that the bubble number is conserved in time. Assumption (c) is used for the model closure. Relative motion between the phases has been shown to have minimal impact on linear wave propagation (d'Agostino et al., 1988) and also plays a minor role in shock propagation if the mixture is dilute (Kameda and Matsumoto, 1996; Seo et al., 2010). Assumption (e) is reasonable due to the fact that the velocity fluctuations caused by the bubble dynamics concentrate in the vicinity of the bubbles, where the liquid is effectively incompressible (Prosperetti and Lezzi, 1986).

Under these assumptions, we write the ensemble-averaged equations as

$$\frac{\partial \rho}{\partial t} + \nabla \cdot (\rho \mathbf{u}) = 0, \tag{1}$$

$$\frac{\partial \rho \mathbf{u}}{\partial t} + \nabla \cdot [\rho \mathbf{u}\mathbf{u} + (p_l - \tilde{p})\mathbf{I}] = 0, \tag{2}$$

$$\frac{\partial \alpha}{\partial t} + \nabla \cdot (\alpha \mathbf{u}) = 3\alpha \frac{\overline{R^2 \dot{R}}}{\overline{R^3}}, \tag{3}$$

where ρ is the mixture density, $\mathbf{u}$ is the mixture velocity, p_l is the averaged liquid pressure, $\mathbf{I}$ is the identity tensor, α is the void fraction, R is the bubble radius, and $\dot{R}$ is the bubble wall velocity. For dilute cases, the mixture density is well approximated by $(1 - \alpha)\rho_l$, where ρ_l is the liquid density. The averaged liquid pressure may be described by the Tait equation of state (Thompson, 1972),

$$\frac{p_l + B}{p_{l0} + B} = \left(\frac{\rho_l}{\rho_{l0}}\right)^m = \frac{1}{\rho_{l0}^m}\left(\frac{\rho}{1 - \alpha}\right)^m, \tag{4}$$

where ρ_{l0} is the reference liquid density at the ambient pressure p_{l0}, and m and B denote stiffness and tensile strength of the liquid, respectively.

The term $\tilde{p}$ in the momentum flux in Eq. (2) represents pressure fluctuations due to the phase interactions,

$$\tilde{p} = \alpha \left(p_l - \frac{\overline{R^3 p_{bw}}}{\overline{R^3}} - \rho \frac{\overline{R^3 \dot{R}^2}}{\overline{R^3}} \right), \tag{5}$$

where p_{bw} is the bubble wall pressure described by the dynamic boundary condition (Brennen, 1995),

$$p_{bw} = p_b - \frac{4\mu_l \dot{R}}{R} - \frac{2\Upsilon}{R}. \tag{6}$$

Here, p_b is the internal bubble pressure (sum of noncondensible gas pressure p_g and vapor pressure p_v), μ_l is the liquid viscosity, and Υ is the surface tension.

The overbar in Eqs. (3) and (5) denotes moments with respect to the (normalized) distribution of equilibrium bubble sizes, $f(R_0)$,

$$\bar{\varphi}(\mathbf{x}, t) = \int_0^\infty \varphi(\mathbf{x}, t; R_0) f(R_0) dR_0, \tag{7}$$

where R_0 is the equilibrium bubble radius corresponding to the ambient pressure and φ represents any of $R^2 \dot{R}$, $R^3 p_{bw}$, $R^3 \dot{R}^2$ or R^3. Note that the functional dependence of R_0 on the distribution is assumed spatially uniform. This assumption is valid for all times due to the no-slip assumption (d). For example, the void fraction is defined as

$$\alpha = \frac{4\pi}{3} n \overline{R^3}, \tag{8}$$

where n is the number of bubbles per unit volume of the mixture and is conserved in time because of the assumption (a); namely

$$\frac{\partial n}{\partial t} + \nabla \cdot (n\mathbf{u}) = 0. \tag{9}$$

It should be noted that the phase interaction term $\tilde{p}$ does not appear in the volume-averaged momentum equation of van Wijngaarden (1968, 1972). However, for linearized dynamics of the bubbles, the momentum Eq. (2) will reduce to van Wijngaarden's equation in the dilute limit. It is also instructive to point out that Eq. (2) coincides with the averaged momentum equation of Biesheuvel and van Wijngaarden (1984) or Zhang and Prosperetti (1994) with no-slip and monodisperse assumptions.

2.1.2. Model distribution of equilibrium bubble sizes

We model the distribution of equilibrium bubble sizes using a lognormal function with the probable size R_0^{ref} and standard deviation σ,

$$f(R_0^*) = \frac{1}{\sqrt{2\pi}\sigma R_0^*} \exp\left(-\frac{\ln^2 R_0^*}{2\sigma^2}\right), \tag{10}$$

where $R_0^* = R_0/R_0^{\text{ref}}$. The lognormal function (10) approaches zero exponentially in the limit of $\ln R_0^* \to \infty$, so that contributions of extremely large sizes, which may deteriorate the continuum model accuracy, to integration (7) can be minimized. In the limit of

$\sigma \to 0$, the function (10) reduces to the Dirac delta function, which models monodisperse mixtures.

Fig. 1 shows the measured nuclei size distributions in a water tunnel (Katz, 1978) and the ocean (O'Hern et al., 1988), together with the lognormal function (10). It follows that $\sigma = 0.7$ may be a reasonable value to model the actual distributions in engineering flows and the ocean, but we use the distribution (10) as illustrative of the qualitative effects of polydispersity rather than to model a particular system. The numerical method developed in Section 3 is independent of this choice, and an empirically determined distribution could easily be employed in future computations.

2.1.3. Model limitations

We now discuss specific limitations associated with assumptions (a) and (b) in Section 2.1.1, which are essential for deriving the continuum model.

The spherical-bubble assumption (a) implies no fission of the bubbles. Possible mechanisms responsible for the fission are a re-entrant jet and a Rayleigh–Taylor-type instability (Brennen, 2002). If the thickness of the incident shock is comparable to or smaller than the bubble sizes, the bubbles distort nonspherically and may finally result in fission due to the re-entrant jet. However, the interaction of the averaged pressure field and the bubble cloud is known to broaden the shock thickness. As a result, the bubble fission does not occur frequently if the shock strength is sufficiently small (Beylich and Gülhan, 1990). For strong shocks, the bubble collapse is so violent that nonspherical distortions arise and fission is likely (Ando et al., 2011). It should be mentioned that Delale and Tunç (2004) made an effort to account for the fission damping in Rayleigh–Plesset calculations, based on the analysis of Brennen (2002).

For assumption (b) to be valid, the mean bubble spacing ($l = n^{-1/3}$) must be much larger than the bubble sizes; the mixture needs to be dilute. The acoustic theory of linear waves in monodisperse bubbly liquids is known to overestimate attenuation under the resonant condition since the bubble/bubble interactions can never be ignored even in the dilute limit (Waterman and Truell, 1961). Inclusion of the broad size distribution can de-emphasize errors associated with resonance since the probability that a bubble of certain size is under resonance is low among a broad spectrum of R_0 (Feuillade, 1996). In Section 4.3, we examine the effect of the bubble/bubble interactions on the shock
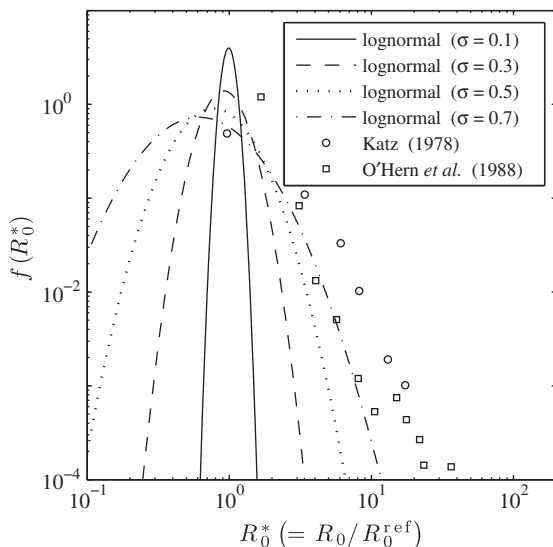

Fig. 1. Normalized distributions of the equilibrium bubble radius. The probable size, R_0^{ref}, is set to 10 μm.

dynamics by comparing the continuum flow simulaiton to the direct numerical simulation of Seo et al. (2010).

2.2. Single-bubble-dynamic model

2.2.1. Model assumptions

In order to close the continuum model, there is a need to solve the single bubble dynamics, but the detailed conservation equations of both the liquid phase and the bubble contents are computationally expensive. This necessitates employing a Rayleigh–Plesset-type equation with the following simplifications: (f) the bubble contents (noncondensible gas and vapor) have spatially uniform pressure; (g) the bubble contents are perfect; (h) the liquid is cold (far from the boiling point); (i) the mass of noncondensible gas in the bubble is unchanged; (j) phase change occurs instantaneously; (k) Fick's law holds for mass diffusion between the noncondensible gas and the vapor; and (l) the transport properties of the bubble contents are constant.

The homobaric assumption (f) is valid since the inertia of the bubble contents is negligible compared to that of the liquid. The cold liquid assumption (h) leads to undisturbed liquid temperature at the bubble wall, so that the energy equation in the liquid phase is unnecessary to solve (Prosperetti et al., 1988). The typical bubble growth rate due to mass transfer of dissolved air in water is so slow (compared to the bubble oscillation rate) that assumption (i) is reasonable (Plesset and Prosperetti, 1977). Assumptions (h) and (j) imply constant vapor pressure at the bubble wall, which is typically adequate except near the end of a violent bubble collapse (Fujikawa and Akamatsu, 1980).

2.2.2. The Gilmore equation

The equation of Gilmore (1952),

$$R\ddot{R}\left(1 - \frac{\dot{R}}{C}\right) + \frac{3}{2}\dot{R}^2\left(1 - \frac{\dot{R}}{3C}\right) = H\left(1 + \frac{\dot{R}}{C}\right) + \frac{R\dot{H}}{C}\left(1 - \frac{\dot{R}}{C}\right), \quad (11)$$

is used to evaluate the spherical bubble dynamics. Here, the dot denotes the substantial time derivative, and H and C are the enthalpy and the sonic speed, respectively, at the bubble wall in the liquid:

$$H = \int_{p_l}^{p_{bw}} \frac{dp_l'}{\rho_l(p_l')}, \quad C = \left(\frac{dp_l}{d\rho_l}\bigg|_{p_l=p_{bw}}\right)^{\frac{1}{2}}. \quad (12)$$

In the dilute limit, the averaged liquid pressure p_l can be considered to be pressure far from the bubble (van Wijngaarden, 1968, 1972; Caflisch et al., 1985a; Takahira, 2004).

2.2.3. Equations for bubble contents

Consider the bubble energy equation, which is coupled to the Gilmore Eq. (11). The rate of the bubble energy change equals the sum of work done by the bubble wall and energy transfered due to the mass flux of vapor and the heat flux at the bubble wall; namely

$$\frac{d}{dt}\int_0^{R(t)} (\rho_g e_g + \rho_v e_v)4\pi r'^2 dr' = 4\pi R^2\left(-\dot{R}p_b + c_{pv}T_w \dot{m}_v'' + k_{bw}\frac{\partial T}{\partial r}\bigg|_w\right), \tag{13}$$

where the subscripts g, v, b and w denote noncondensible gas, vapor, bubble contents and bubble wall properties, respectively, e is the internal energy, c_p is the specific heat at constant pressure, T_w is the bubble wall temperature, $\dot{m}''$ is the mass flux, k is the thermal conductivity, T is the temperature, and r is the radial coordinate measured from the bubble center.

With assumptions (f) and (g), Eq. (13) reduces to the following equation (Nigmatulin et al., 1981; Prosperetti et al., 1988),

$$\dot{p}_b = \frac{3\gamma_b}{R}\left(-\dot{R}p_b + \Re_v T_w \dot{m}_v'' + \frac{\gamma_b - 1}{\gamma_b}k_{bw}\frac{\partial T}{\partial r}\bigg|_w\right), \tag{14}$$

where γ_b is the specific-heat ratio of the bubble contents and $\Re$ is the gas constant. In the derivation, it is assumed that the specific ratio of noncondensible gas, γ_g, is nearly the same as that of vapor, γ_v (i.e., $\gamma_b \approx \gamma_g \approx \gamma_v$). The thermal conductivity for the bubble contents, k_b, is taken from a semi-empirical formula (Bird et al., 1960). For efficient computations, the heat and vapor fluxes at the bubble wall are estimated using the reduced-order model of Preston et al. (2007), which has been shown to be accurate for small bubbles.

It should be noted that the polytropic gas obeys

$$p_b = p_v + p_{g0}\left(\frac{R}{R_0}\right)^{-3\kappa}, \tag{15}$$

where p_{g0} is the partial pressure of the noncondensible gas in the equilibrium state and κ is the polytropic index; $\kappa = 1$ implies constant bubble temperature and $\kappa = \gamma_g$ would model adiabatic behavior. In this case, Eq. (14) is unnecessary to solve. In Sections 4.2 and 4.3, the polytropic relation (15) is used; otherwise, Eq. (14) with the transfer model of Preston et al. (2007) is solved to account for diffusive effects on the bubble dynamics.

2.2.4. The conservation form

We now write the bubble-dynamic equations in a conservation form, which is suitable for shock computations (LeVeque, 1992):

$$\frac{\partial n\varphi}{\partial t} + \nabla \cdot (n\varphi \mathbf{u}) = n\dot{\varphi}. \tag{16}$$

In this form, the bubble-dynamic variables, φ, are treated as Eulerian variables (i.e., $\varphi = \varphi(\mathbf{x},t;R_0)$) rather than Lagrangian particles (Watanabe and Prosperetti, 1994). Since we assume a large number of the bubbles in mixtures, the bubbles may be considered to be distributed continuously in space. If we evaluate the heat and vapor fluxes using Preston's model, the bubble pressure p_b and the mass of vapor m_v (in addition to R and $\dot{R}$) need to be included in φ.

2.3. The complete system

For simplicity, we write the resulting system in one dimension using a vector form:

$$\mathbf{q}_t + \mathbf{f}(\mathbf{q})_x = \mathbf{f}^s(\mathbf{q})_x + \mathbf{s}(\mathbf{q}), \tag{17}$$

where the subscript denotes partial derivatives. The column vectors are

$$\mathbf{q} = \begin{Bmatrix} \rho \\ \rho u \\ \alpha \\ n\varphi \end{Bmatrix}, \quad \mathbf{f} = \begin{Bmatrix} \rho u \\ \rho u^2 + p_l \\ \alpha u \\ n\varphi u \end{Bmatrix}, \quad \mathbf{f}^s = \begin{Bmatrix} 0 \\ \tilde{p} \\ 0 \\ 0 \end{Bmatrix}, \quad \mathbf{s} = \begin{Bmatrix} 0 \\ 0 \\ 3\alpha\frac{R^2\dot{R}}{R^3} \\ n\dot{\varphi} \end{Bmatrix}, \tag{18}$$

where u is the x-component velocity. Note that the sources, $\mathbf{f}^s$ and $\mathbf{s}$, vanish in the equilibrium state. In this expression, φ is treated, for simplicity, as a scalar quantity and represents any of the bubble-dynamic variables. However, if one shows the entire system, the scalar φ needs to be replaced with its column vector version that consists of all the bubble-dynamic variables.

The quasilinear form of Eq. (17) is

$$\mathbf{q}_t + \mathbf{A}\mathbf{q}_x = \mathbf{f}^s(\mathbf{q})_x + \mathbf{s}(\mathbf{q}), \tag{19}$$

where $\mathbf{A}$ is the Jacobian matrix ($\partial\mathbf{f}/\partial\mathbf{q}$). The eigenvalues of $\mathbf{A}$ are

$$\lambda_1 = u - \tilde{c}_l, \quad \lambda_2 = u + \tilde{c}_l, \quad \lambda_3 = \lambda_4 = u. \tag{20}$$

Here, $\tilde{c}_l = c_l/(1 - \alpha)$ where c_l is the sonic speed of the (Tait) liquid. The matrix of the right eigenvectors (satisfying $\mathbf{A}\mathbf{r}_i = \lambda_i\mathbf{r}_i$) of $\mathbf{A}$ is

$$\mathbf{R} = [\mathbf{r}_1 \ \mathbf{r}_2 \ \mathbf{r}_3 \ \mathbf{r}_4] = \begin{bmatrix} \rho & \rho & \rho & 0 \\ \rho(u - \tilde{c}_l) & \rho(u + \tilde{c}_l) & \rho u & 0 \\ \alpha & \alpha & \alpha - 1 & 0 \\ n\varphi & n\varphi & 0 & 1 \end{bmatrix}, \tag{21}$$

where the fields associated with $\mathbf{r}_3$ and $\mathbf{r}_4$ represent the contact waves across which u and p_l are continuous but ρ, α and $n\varphi$ are discoutinuous (Toro, 1999). Correspondingly, the matrix of the left eigenvectors (satisfying $\mathbf{l}_i\mathbf{A} = \lambda_i\mathbf{l}_i$) of $\mathbf{A}$ is

$$\mathbf{L} = \begin{bmatrix} \mathbf{l}_1 \\ \mathbf{l}_2 \\ \mathbf{l}_3 \\ \mathbf{l}_4 \end{bmatrix} = \begin{bmatrix} \frac{u+(1-\alpha)\tilde{c}_l}{2\rho\tilde{c}_l} & \frac{-1}{2\rho\tilde{c}_l} & \frac{1}{2} & 0 \\ \frac{-u+(1-\alpha)\tilde{c}_l}{2\rho\tilde{c}_l} & \frac{1}{2\rho\tilde{c}_l} & \frac{1}{2} & 0 \\ \frac{\alpha}{\rho} & 0 & -1 & 0 \\ \frac{(\alpha-1)n\varphi}{\rho} & 0 & -n\varphi & 1 \end{bmatrix}. \tag{22}$$

The right and left eigenvectors (21) and (22) are used for the transformation from the conserved to the characteristic variables (i.e., $\mathbf{p} = \mathbf{L}\mathbf{q}$) or from the characteristic to the conserved variables (i.e., $\mathbf{q} = \mathbf{R}\mathbf{p}$). We note that if the scalar φ is replaced with its vector version, the unity at the lower right corner of the matrices (21) and (22) should be interpreted as an identity sub-matrix.

2.4. Ensemble and volume averaging

Here, we consider the relation between ensemble and volume averages. The concept of volume averaging is to average quantities within a control volume of mixtures with specific, instantaneous realizations of bubbly flows. For example, with the control volume $\mathcal{V}$ consisting of the liquid-phase and gas-phase volumes (i.e., $\mathcal{V} = \mathcal{V}_l + \mathcal{V}_g$), the dilute mixture density ρ can be defined as

$$\rho = \frac{\mathcal{V}_l\rho_l + \mathcal{V}_g\rho_g}{\mathcal{V}} \approx \frac{\mathcal{V}_l\rho_l}{\mathcal{V}}. \tag{23}$$

In order that the mixture within $\mathcal{V}$ be considered homogeneous and the averaged wave structure be well resolved, we need to choose an appropriate averaging volume and presuppose the scale separation (Nigmatulin, 1979; Prosperetti, 2001):

$$l = n^{-\frac{1}{3}} \ll \mathcal{V}^{\frac{1}{3}} \ll L, \tag{24}$$

where l is the mean bubble spacing and L is the (averaged) wavelength in the mixture. On the other hand, in ensemble averaging, we need not presuppose such a scale separation for deriving the averaged equations. However, the scale separation assumption is ultimately still needed for the model closure.

Under the scale separation (24), the system can be considered homogeneous locally in space and the equality between ensemble and volume averages will thus hold (Batchelor, 1970; Biesheuvel and van Wijngaarden, 1984). In other words, if the wavelength of interest is large enough to satisfy the scale separation, the ensemble-averaged quantities will be equivalent to the volume averages. This observation is consistent with the fact that the ensemble-averaged equations in Section 2.1.1 are essentially the same as van Wijngaarden's volume-averaged equations.

It is also instructive to mention the analysis of d'Agostino and Brennen (1989). They considered the dynamics of a spherical (monodisperse) bubble cloud with radius R_c, under sinusoidal pressure forcing, with the implicit assumption that the cloud dimension is far smaller than the wavelength associated with the pressure forcing (i.e., $R_c \ll L$). That is, their cloud size corresponds to the dimension of the control volume, $\mathcal{V}^{1/3}$, in Eq. (24). A linear analysis reveals that the cloud has an infinite set of natural frequencies:

$$\omega_i = \omega_N \left[1 + \frac{12\beta}{(2i-1)^2 \pi^2} \right]^{-\frac{1}{2}}, \tag{25}$$

where i is positive integers, ω_N is the natural frequency of individual bubble oscillations, and β is termed the *cloud interaction parameter* defined as

$$\beta = \frac{\alpha_0(1-\alpha_0)R_c^2}{R_0^2}. \tag{26}$$

The lowest natural frequency, ω_1, can be much smaller than ω_N if β is far larger than unity. In the limit of $\beta \to 0$, on the contrary, the cloud interaction effect is minimized and all the bubbles tend to oscillate freely with ω_N. Namely, this parameter governs the extent of bubble/bubble interactions through the averaged field.

With the aid of β, we revisit the scale separation problem. Now that $\mathcal{V}^{-1/3}$ can be replaced with R_c, the relation (24) reads

$$\alpha_0^{\frac{1}{3}} \ll \beta \ll \left(\frac{L}{R_0^{\text{ref}}} \right)^2 \alpha_0. \tag{27}$$

Provided that there exists the value of β that satisfies the above relation, we can suitably choose an averaging volume in instantaneous realizations of bubbly flows. In this case, the ensemble and volume averages will again be equivalent.

2.5. One-way-coupled flow computations

Before proceeding to two-way-coupled flow computations, we consider the evolution of moments (7) in the one-way-coupling case ($\beta \to 0$) where any bubble/bubble interactions are neglected. Specifically, our interest is to predict the moments of bubble radius with respect to the lognormal distribution (10):

$$\mu_i(\mathbf{x}, t) = \int_0^\infty R^i(\mathbf{x}, t; R_0) f(R_0) dR_0. \tag{28}$$

For example, the third moment $\mu_3(\mathbf{x}, t)$ represents the mean bubble volume. In the volume-averaging sense, $\mu_3(\mathbf{x}, t)$ can be interpreted as the mean bubble volume within an averaging volume $\mathcal{V}$ centered at $\mathbf{x}$.

We now consider the problem that air/vapor bubbles in water are initialized with the distribution (10) at standard temperature and pressure (STP; 20 °C and 101 kPa) and then forced according to a step-wise pressure change from p_{l0} to $2p_{l0}$ at $t = 0$. This may be a simple example to shock propagation in bubbly flows. The bubble dynamics are computed by integrating the inviscid Rayleigh–Plesset equation with isothermal air. The physical properties are taken from Lide (2006).

Fig. 2 shows the integrand of the third moment μ_3, at three different times, for the lognormal distribution with $R_0^{\text{ref}} = 10$ μm and $\sigma = 0.7$. Time is normalized by the time scale, $R_0^{\text{ref}} \sqrt{\rho_{l0}/p_{l0}}$. It is seen that the integrand becomes more oscillatory as the bubble oscillations evolve, because the bubbles with different equilibrium sizes oscillate with different frequencies; eventually, the different-sized bubbles oscillate totally out of phase. In Fig. 3, the evolution of the third moment $\mu_3(t^*)$ is presented. It transpires that the inviscid bubble oscillations in the polydisperse case achieve a time-invariant value of the moment even though all the bubbles keep oscillating without any damping. We say that the bubble oscillations reach a *statistical equilibrium* due to phase cancellations among bubbles with different sizes. The existence of the statistical equilibrium is mathematically proven by Colonius et al. (2008). At the statistical equilibrium, the polydisperse bubble cloud does not oscillate in volume, regardless of oscillations of the individual bubbles. Thus, the cancellation effect can be regarded as an *apparent* damping of the averaged dynamics.

3. Numerical method

3.1. Spatial discretization

3.1.1. Finite-volume reconstruction

Since shocks in bubbly flows often have oscillatory structures that result from bubble dynamics, we favor the properties of high-order accurate resolution in complex smooth structures as well as shock capturing. Herein, we choose a finite-volume (FV) weighted essentially non-oscillatory (WENO) scheme (Liu et al., 1994), which contains such properties in addition to robustness, with monotonicity preserving bounds (Balsara and Shu, 2000). To guarantee essentially non-oscillatory solutions, it is safe to implement the WENO reconstruction in characteristic space even though a local characteristic decomposition is computationally expensive (Qiu and Shu, 2002).

Given a computational cell $[x_{i-1/2}, x_{i+1/2}]$ where i denotes the grid index, the system (17) is discretized in FV fashion:

$$\frac{d\bar{\mathbf{q}}_i}{dt} = -\frac{\mathbf{f}_{i+1/2} - \mathbf{f}_{i-1/2}}{\Delta x_i} + \frac{\mathbf{f}_{i+1/2}^s - \mathbf{f}_{i-1/2}^s}{\Delta x_i} + \bar{\mathbf{s}}_i, \tag{29}$$

where the overbar denotes the cell-averaged quantities. In FV methods, $\bar{\mathbf{q}}_i$ is reconstructed at each cell edge, and the numerical flux $\mathbf{f}_{i+1/2}$ is computed by solving a local Riemann problem.

3.1.2. HLLC approximate Riemann solver

To compute the numerical fluxes ($\mathbf{f}_{i+1/2}$ and $\mathbf{f}_{i+1/2}^s$), we use the HLLC approximate Riemann solver (Toro et al., 1994). If the left and right states ($\mathbf{q}^L, \mathbf{q}^R$) are imposed at $x = 0$ and $t = 0$, the HLLC Riemann solution is given by

$$\mathbf{q}^{\text{HLLC}}(x, t) = \begin{cases} \mathbf{q}^L & \text{if } x/t \leqslant s^L, \\ \mathbf{q}^{*L} & \text{if } s^L \leqslant x/t \leqslant s^*, \\ \mathbf{q}^{*R} & \text{if } s^* \leqslant x/t \leqslant s^R, \\ \mathbf{q}^R & \text{if } x/t \geqslant s^R. \end{cases} \tag{30}$$

The Rankine–Hugoniot conditions across the contact waves (constructed for the hyperbolic part) yield the expression for the intermediate (star) state:

$$\mathbf{q}^{*K} = \frac{s^K - u^K}{s^K - s^*} \begin{Bmatrix} \rho^K \\ \rho^K s^* \\ \alpha^K \\ (n\varphi)^K \end{Bmatrix}, \tag{31}$$

where K = L or R. It follows from Einfeldt et al. (1991) that

$$s^L = \min\left((u - \tilde{c}_l)^{\text{Roe}}, u^L - \tilde{c}_l^L \right), \quad s^R = \max\left((u + \tilde{c}_l)^{\text{Roe}}, u^R + \tilde{c}_l^R \right), \tag{32}$$

where the superscript "Roe" stands for the Roe averages (Roe, 1981). The intermediate wave speed (Batten et al., 1997) is

$$s^* = \frac{p_l^R - p_l^L + \rho^L u^L (s^L - u^L) - \rho^R u^R (s^R - u^R)}{\rho^L (s^L - u^L) - \rho^R (s^R - u^R)}. \tag{33}$$

3.2. Time marching

Given the HLLC fluxes and the sources, the system written in a semi-discrete form can be integrated in time. The simplest way is to employ explicit methods in which a single time step Δt is used to resolve both the convective and the bubble-dynamic terms. A third-order TVD Runge–Kutta scheme (Shu and Osher, 1988) is often used for stable shock computations. The choice of Δt depends on the constraint on the dimensionless Courant–Friedrichs–Lewy (CFL) number (LeVeque, 1992; Toro, 1999), which is defined as
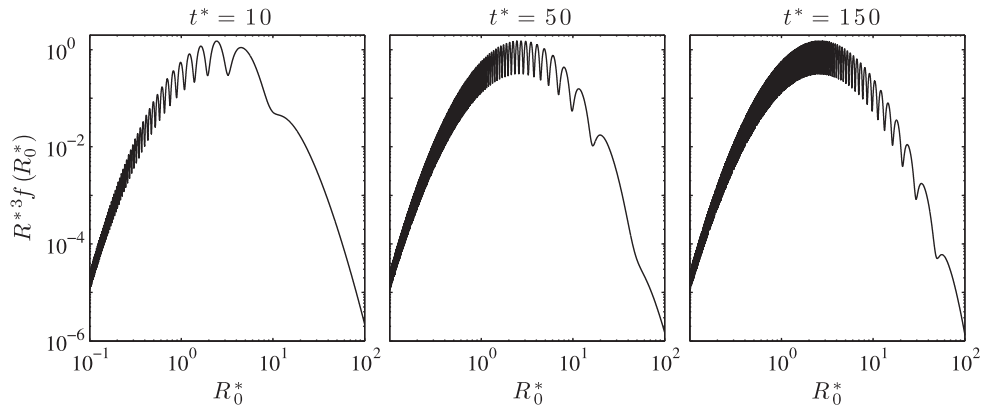
Fig. 2. Integrand of the third moment μ_3 for the inviscid oscillations of bubbles at different times. The equilibrium bubble size is assumed lognormally distributed with $R_0^{\mathrm{ref}} = 10 \, \mu m$ and $\sigma = 0.7$.
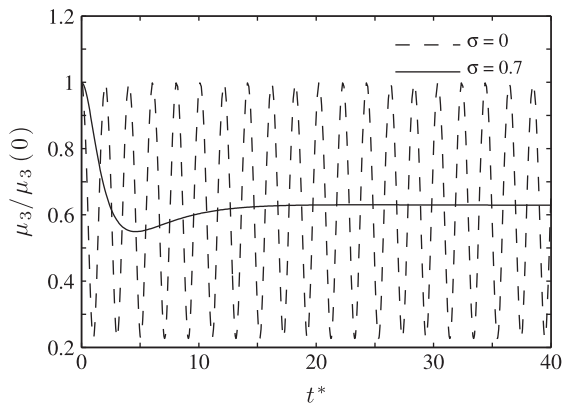

Fig. 3. Evolution of μ_3 for the inviscid oscillations of bubbles.

the ratio of the physical wave speed to the grid speed $\Delta x_i/\Delta t$. For one-dimensional computations, the maximum CFL number may be defined as

$$\mathrm{CFL} = \Delta t \max_i \left\{ \frac{|u_i| + (\tilde{c}_l)_i}{\Delta x_i} \right\}. \tag{34}$$

For hyperbolic systems, a linear analysis shows that the CFL constraint is given by $0 < \mathrm{CFL} \leqslant 1$. However, the system (17) is not rigorously hyperbolic, and the bubble dynamics would alter the stability condition.

3.3. Nonreflective boundary condition

The treatment of nonreflective boundaries is based on the work of Thompson (1987). His idea is to evaluate only outgoing waves from a finite computational domain at the boundaries. For computations of bubbly flows, the sonic speed evaluation at the boundaries is intractable because the waves are dispersive. For shock computations in Section 4, the sonic speed of mixtures in a low frequency limit (see for example Brennen (1995)) is used for the sonic speed evaluation:

$$c = \sqrt{\frac{m(p_l + B)}{\rho} \frac{\kappa p_l}{\alpha m(p_l + B) + (1 - \alpha)\kappa p_l}}. \tag{35}$$

However, in this manner, high-frequency waves can be reflected back into the computational domain. The domain is thus set to be large enough that the spurious waves do not contaminate the solution of interest.

3.4. Verification

As a verification test, we solve one-dimensional linear wave propagation in an air/water mixture of $\alpha_0 = 0.001$ at STP. Since the vapor pressure is much smaller than the ambient pressure, the vapor flux in Eq. (14) is omitted. To see wave dispersion, we impose the following initial condition,

$$p_l(x) = p_{l0} \left[1 + \epsilon \exp \left(-\frac{x^2}{h^2} \right) \right], \quad u_l(x) = 0, \tag{36}$$

where $\epsilon = 10^{-4}$ and $h = 4R_0^{\mathrm{ref}}$. The equilibrium bubble size is assumed lognormally distributed about $R_0^{\mathrm{ref}} = 10 \, \mu m$. The fifth-order monotonicity-preserving FV-WENO reconstruction is implemented in the characteristic space and the HLLC Riemann solver manipulates the numerical flux. The computational grid is uniform with $\Delta x = R_0^{\mathrm{ref}}$. The time marching is handled using the third-order TVD Runge–Kutta scheme with CFL = 0.1. For the polydisperse case, the moment (7) is evaluated using Simpson's rule with 101 quadrature points.

Fig. 4 shows the averaged liquid pressure distribution at $t = 11.2 \, \mu s$ in the monodisperse mixture ($\sigma = 0$) or polydisperse mixture ($\sigma = 0.7$). As in the experiment of Kuznetsov et al. (1978), we observe wave dispersion due to bubble dynamics. Specifically, the high-wavenumber waves propagate essentially with the sonic speed of water alone, c_{l0}, but the waves with low wavenumbers propagate more slowly. Note that the bubble size distribution with $\sigma = 0.7$ smoothes out the oscillatory structure in the low-wavenumber signal.
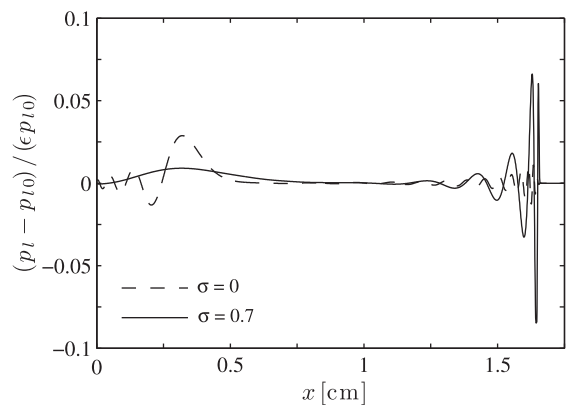

Fig. 4. Spatial evolution of the averaged liquid pressure at $t = 11.2 \, \mu s$ for linear wave propagation in an air/water mixture of $\alpha_0 = 0.001$ and $R_0^{\mathrm{ref}} = 10 \, \mu m$ at STP.

To verify the present model, the phase velocity and attenuation of the linear waves are computed from the numerical experiment (as explained in Appendix A) and compared to the acoustic theory (Ando et al., 2009). Fig. 5 compares the computed phase velocity and attenuation to the theoretical predictions. Quantitative agreement in a wide range of frequency totally verifies the present method. We also note that the waves with low and high wavenumbers in Fig. 4 correspond to the low-frequency (quasistatic) and high-frequency (ultrasonic) regimes, respectively. The slight deviations from the theory result from the reduced-order model of Preston et al. (2007) for evaluating heat conduction at the bubble wall since Preston's model is never exact for finite values of the Peclet number, which is defined as $\mathrm{Pe} = \omega_N R_0^{\mathrm{ref}2}/\alpha_T$ where α_T is the thermal diffusivity of the bubble contents.

We now revisit the scale separation discussion (in Section 2.4) to examine the continuum assumption. In this example, Eq. (27) now reads

$$0.1 \ll \beta \ll 0.001 \left(\frac{L}{R_0^{\mathrm{ref}}} \right)^2. \tag{37}$$

For the right-hand side to be two orders of magnitude larger than 0.1, we need large wavelengths to satisfy $L/R_0^{\mathrm{ref}} \gtrsim 100$. The low-wavenumber waves reasonably meet this constraint; thus, we can suitably choose an averaging control volume with $\beta \approx 1$ to define volume averages, which will be equivalent to ensemble averages. However, the high-wavenumber waves are larger than the bubble dimensions but comparable to the mean bubble spacing (≈ 0.16 mm for $\sigma = 0$); the scale separation (37) does not hold and the continuum approach itself is invalid. In summary, the continuum model is applicable to low-frequency waves in the quasistatic regime but is less accurate in ultrasonic wave solutions.

Finally, we consider the corresponding one-way-coupled problem in order to quantify the two-way-coupling effect. Provided that the cloud interaction is minimized, the two-way-coupled problem at $x = 0$ may reduce to the one-way-coupling case in which bubble dynamics are excited by impulsive pressure forcing and all the bubbles are oscillating independently with their natural frequencies $\omega_N(R_0)$. Our concern is to predict the second moment of the perturbed bubble radius with respect to the lognormal distribution (10) with $\sigma = 0.7$,

$$\mu_2'(t) = \int_0^\infty [R(t; R_0) - R_0]^2 f(R_0) dR_0, \tag{38}$$

whereas the first moment μ_1' vanishes at the statistical equilibrium (Colonius et al., 2008). For the one-way-coupled flow computation,

the bubble dynamics are computed by integrating the Gilmore equation with the pressure impulse.

Fig. 6 presents the integrands of μ_2' at $t = 10$ μs. For the two-way-coupling case, we plot the integrand at $x = 0$ where the pressure perturbation is initially imposed. In the inviscid and one-way-coupling case, the bubbles of any size keep oscillating with $\omega_N(R_0)$ and their oscillations give rise to a very oscillatory integrand. In the viscous cases, on the contrary, oscillations of the small bubbles are damped down before the integrands become very oscillatory as in the inviscid case, but there still appear phase cancellations among the bubbles of larger sizes. These phase cancellations lead to an apparent damping of low-frequency wave propagation and augment the attenuation as seen in Fig. 5 (Ando et al., 2009). It should be noticed that the two-way-coupling effect lowers the oscillation frequencies so that the integrand becomes less oscillatory.

In Fig. 7, the quadrature errors in computing μ_2' at $t = 10$ μs are plotted by comparing the values of the integral using Simpson's rule (with varying the number of quadrature points N) to their values using a far larger number. This suggests that the moment in the two-way-coupled viscous flow computation can be predicted with fewer quadrature points than in the one-way-coupling cases. This is consistent with the observation in Fig. 6 that the viscous and cloud effects make the integrand less oscillatory. Furthermore, in the two-way-coupling case, 0.1% accuracy is achieved at $N = 101$. However, in practical calculations where 0.1% accuracy is too demanding, one can further decrease N.

3.5. Summary of the numerical implementation

In this section, the high-order-accurate FV method was developed to resolve the wave dispersion. For shock computations in Section 4, the fifth-order monotonicity-preserving FV-WENO reconstruction is implemented in the characteristic space and the HLLC Riemann solver is used to compute the numerical flux. The computational grid is uniform with $\Delta x = R_0^{\mathrm{ref}}$. The third-order TVD Runge–Kutta scheme with CFL = 0.1 is used to march the entire system. For the polydisperse case, Simpson's rule is employed to evaluate the moment (7); 401 quadrature points are used for bubble screen computations in Section 4.6, but otherwise 101 quadrature points are used.

4. Shock dynamics of bubbly flows

4.1. Steady shock relations

We first derive the steady shock relations that can be employed as initial conditions for shock computations. In front of the shock,
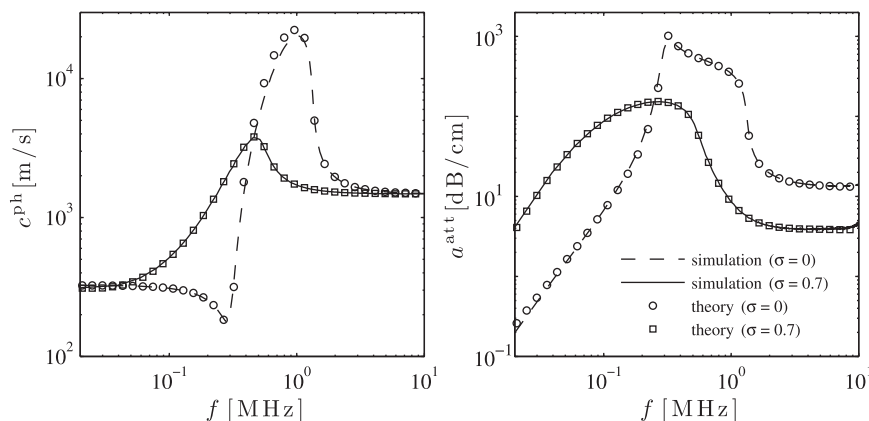

Fig. 5. Phase velocity (left) and attenuation (right) of the linear waves in the air/water mixture. The isothermal natural frequency for $R_0^{\mathrm{ref}} = 10$ μm is 0.291 MHz.
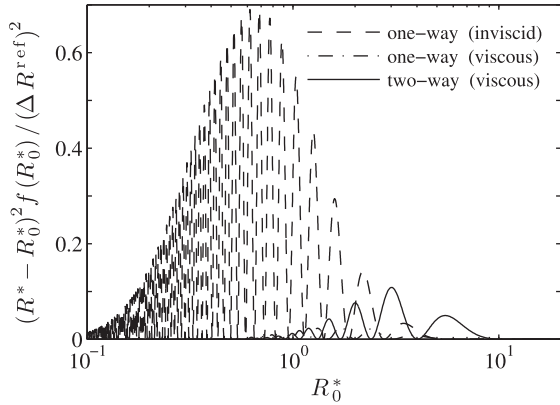
Fig. 6. Integrands of the second moment μ_2' at t = 10 µs. The maximum perturbation, ΔR^{ref}, in bubble radius for $R_0 = R_0^{\mathrm{ref}}$ is used to normalize the integrands.
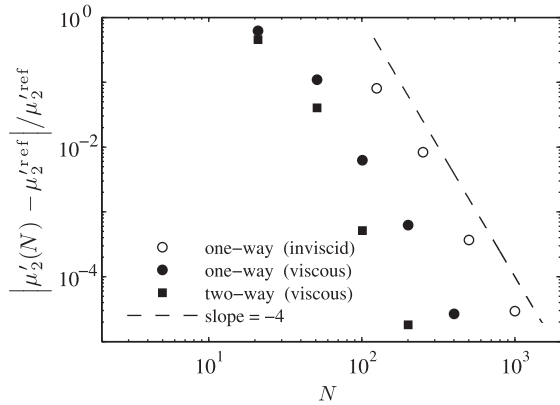

Fig. 7. Quadrature errors for μ_2' at t = 10 µs.

the bubbles are in equilibrium at (R_0, T_0, p_{l0}) where T_0 is the initial temperature of the bubble contents. Far downstream of the shock front, the bubble dynamics are finally damped out and the bubbles are once again in equilibrium at (R_H, T_0, p_{lH}) where R_H is the new equilibrium radius corresponding to the shock pressure p_{lH}. The specification of T_0 in the final equilibrium state follows from the assumption that the liquid temperature is undisturbed and the bubble temperature eventually returns to the liquid temperature. Note that the bubble-dynamic sources would vanish under the equilibrium state. The one-dimensional conservation laws for mass, momentum and bubble number are now written in a coordinate system ($x' = x - U_s t$ and velocity u') moving with the shock velocity U_s:

$$\frac{d\rho u'}{dx'} = 0, \tag{39}$$

$$\frac{d}{dx'}(\rho u'^2 + p_l - \tilde{p}) = 0, \tag{40}$$

$$\frac{dnu'}{dx'} = 0. \tag{41}$$

Integrating Eqs. (39)–(41) from upstream (denoted by the subscript 0) to far downstream (denoted by the subscript H), it transpires that, independent of the detailed shock structure,

$$- \rho_H u_H' = \rho_0 U_s, \tag{42}$$

$$\rho_H u_H'^2 + p_{lH} = \rho_0 U_s^2 + p_{l0}, \tag{43}$$

$$- n_H u_H' = n_0 U_s, \tag{44}$$

where $\rho_0 = (1 - \alpha_0)\rho_{l0}$ and $\rho_{lH} = (1 - \alpha_H)\rho_{lH}$.

The shock pressure, p_{lH}, may be written as

$$p_{lH} = \left(p_{l0} - p_v + \frac{2\Upsilon}{R_0}\right)\left(\frac{R_H}{R_0}\right)^{-3\kappa} + p_v - \frac{2\Upsilon}{R_H}, \tag{45}$$

where the polytropic index κ is set to unity in order that the bubble temperature finally be back to T_0. For adiabatic bubbles, κ needs to be replaced with the specific ratio γ_g. It follows from Eqs. (42) and (44) that

$$n_H = \left[(1 - \alpha_0)\left(\frac{p_{l0} + B}{p_{lH} + B}\right)^{\frac{1}{m}} + \frac{4\pi}{3}n_0\overline{R_H^3}\right]^{-1}. \tag{46}$$

From Eqs. (42) and (43), the steady shock speed becomes

$$U_s = \sqrt{\frac{p_{lH} - p_{l0}}{\rho_0\left(1 - \frac{\rho_0}{\rho_H}\right)}}, \tag{47}$$

and the induced velocity far downstream of the shock front is then given by

$$u_H = u_H' + U_s = \left(1 - \frac{\rho_0}{\rho_H}\right)U_s. \tag{48}$$

It is readily shown that the shock speed (47) reduces to the sonic speed (35) if the shock strength is infinitesimal. Consequently, the shock Mach number may be defined as $M_s = U_s/c$.

4.2. Comparison to experiment

To validate the continuum model, we simulate the experiment of Kameda et al. (1998) in which a spatially uniform bubble distribution was carefully created. We consider shock propagation, with $p_{lH} = 2.157p_{l0}$, in an SF_6/silicone-oil monodisperse mixture of $\alpha_0 = 0.0024$ and $R_0^{\mathrm{ref}} = 0.613$ mm. The corresponding Peclet number is Pe=3770, indicating that the thermal boundary layer inside the bubble is thin compared to the bubble radius. The bubbles thus tend to behave adiabatically; the adiabatic relation (15) with $\kappa = \gamma_g = 1.09$, rather than Eq. (14), is solved. In addition, vapor pressure of the silicone oil at the room temperature is negligible and set to zero. The steady shock relations with $\kappa = \gamma_g$ are initially imposed by a diaphragm at $x = 0$.

The comparison is made in Fig. 8 that shows the time history of the averaged liquid pressure at $x = 1.462$ m. In their experiment, the liquid pressure evolution is averaged over 10 experimental runs. The simulation well reproduces the amplitude and phase of the oscillations in the averaged liquid pressure (so-called relaxation oscillations). The oscillation period τ is about 0.2 ms so that the wavelength is approximately $U_s\tau \approx 6$ cm. On the other hand,
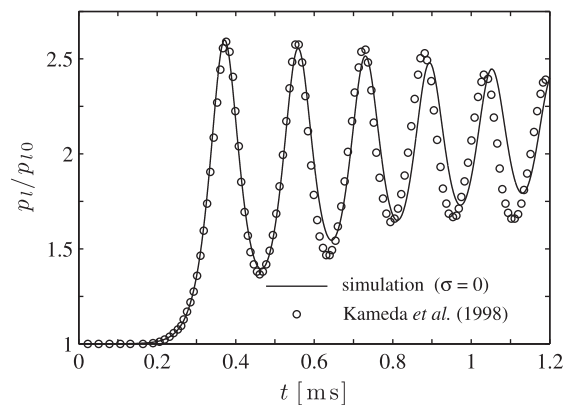

Fig. 8. Evolution of the averaged liquid pressure for shock propagation in an SF_6/silicone-oil mixture of $\alpha_0 = 0.0024$ and $R_0^{\mathrm{ref}} = 0.613$ mm.

the mean bubble spacing is estimated as $n^{-1/3}$ = 7.4 mm. It is therefore concluded that the continuum model is accurate since these length scales satisfy the scale separation constraint.

4.3. Comparison to direct numerical simulaiton

Now that direct numerical simulations (DNS) of shock propagation in a bubbly liquid are available (Delale et al., 2005; Delale and Tryggvason, 2008; Seo et al., 2010), it is easy to examine the effect of direct bubble/bubble interactions on the averaged shock dynamics, by comparison between DNS and continuum flow simulations. As an example, we consider the simulations of Seo et al. (2010) in which the interface between bubbles and a host liquid was captured with the front-tracking method (Tryggvason et al., 2001). In their simulations, the bubbles in an incompressible liquid initially have the same size and are compressed isothermally by a shock. In addition to DNS, continuum flow computations (with or without effects of slip and bubble/bubble interactions) were also conducted for comparison. Their results were characterized by Reynolds and Weber numbers:

$$\mathrm{Re}_R = \sqrt{\frac{p_{l0}}{\rho_{l0}}} \frac{R_0^{\mathrm{ref}}}{\nu_l}, \quad \mathrm{We}_R = \frac{p_{l0} R_0^{\mathrm{ref}}}{\Upsilon},$$

where ν_l is the kinematic viscosity of the liquid.

In Fig. 9, we simulated their case with Re_R = 10, We_R = 13.88, α_0 = 0.00419, $p_{lH} = 1.5 p_{l0}$, and the isothermal relation (15), but with compressible water. In this figure, their results of continuum flow simulation (excluding slip and bubble/bubble interactions) and DNS are also presented. Note that the slip effect was shown to be negligible in this example. The difference in the continuum flow solutions is due to the acoustic damping associated with the compressibility of water, which has limited impact on the averaged shock structure in this particular example. More importantly, the direct interactions between the bubbles are rather effective even when the void fraction is below 0.01. If one considers cases with higher void fractions, there will be a strong need to account for such effects in continuum flow modeling (Caflisch et al., 1985b; Seo et al., 2010). In the following examples, the present work is focused on the shock dynamics of a polydisperse cloud of bubbles in the dilute case (say α_0 = 0.005), rather than going into the more detailed modeling for large values of α_0.

4.4. Effect of polydispersity on shock dynamics

We now consider unsteady and steady shock propagation through a polydisperse bubbly liquid. As an example, we compute
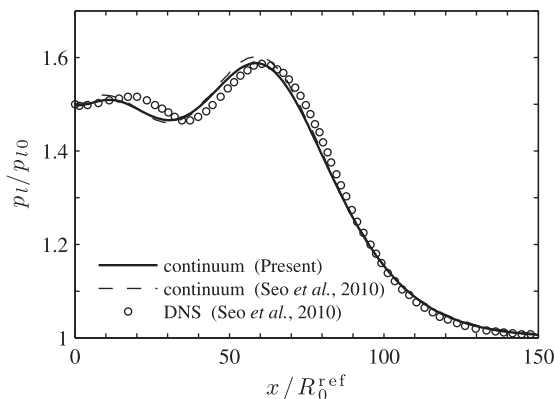
shock propagation, with $p_{lH} = 2 p_{l0}$, in an air/water mixture of α_0 = 0.005 at STP where the equilibrium bubble size is lognormally distributed about $R_0^{\mathrm{ref}} = 10$ μm and with σ ranging from 0 to 0.7. With the isothermal assumption, the corresponding shock Mach number is M_s = 1.4 for all σ. The steady shock relations with $\kappa = 1$ are initially imposed by a diaphragm at $x = 0$. We judge steadiness by observing the first peak of the relaxation oscillations; if the peak pressure is unchanged, the shock propagation is considered to be in a steady state.

4.4.1. Unsteady shock propagation

The unsteady shock propagation for the cases with σ = 0 and 0.7 is investigated in Figs. 10 and 11. In Fig. 11, the spatial evolution of the bubble radius with different R_0 is plotted to interpret the individual bubble dynamics. It is seen that the (high-frequency) precursory pressure wave precedes the primary shock wave and propagates essentially with the sonic speed of (pure) water. Whereas the precursory pressure wave in the monodisperse mixture is damped out, that in the polydisperse case is still on the decay. This may be due to the fact that the bubble size distribution decreases the attenuation of high-frequency waves as seen in Fig. 5. It also turns out that only the small-sized bubbles can respond to such high-frequency excitation, for the natural frequency of such small bubbles is comparable with or higher than the forcing frequency. As observed in the low-frequency regime of the linear waves in Fig. 4, the distribution with σ = 0.7 smoothes the relaxation oscillations in the averaged pressure and void fraction distributions. It should be noticed that the different-sized bubbles oscillate with different phases in the neighborhood of the primary shock front.

Fig. 12 presents the spatial evolution of the averaged liquid pressure and the bubble radius with different R_0 at two different times at which the larger-sized bubbles still show radial oscillations (with less effective bubble-dynamic damping). The shock
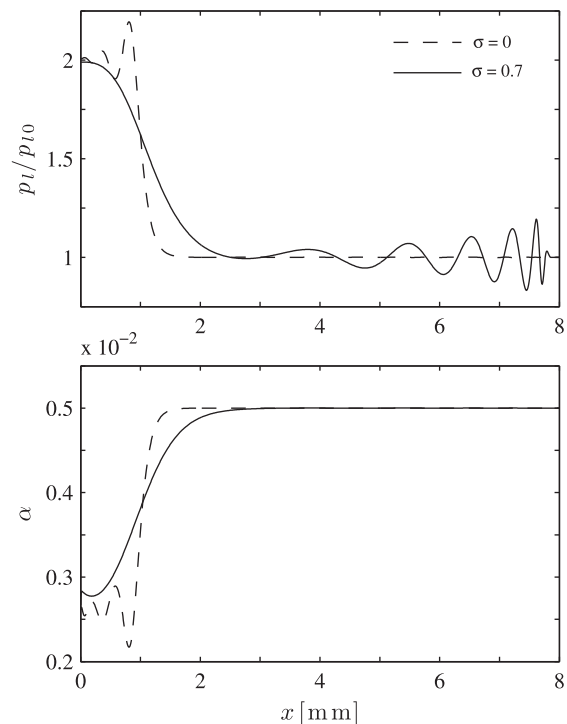
Fig. 9. Spatial evolution of the averaged liquid pressure at t^* = 5 for unsteady shock propagation in an isothermal-gas/liquid mixture of α_0 = 0.00419 at STP. The liquid is assumed to be incompressible in Seo et al. (2010).

Fig. 10. Spatial evolution of the averaged liquid pressure (top) and the void fraction (bottom) at t = 5.2 μs for unsteady shock propagation in an air/water mixture of α_0 = 0.005 and $R_0^{\mathrm{ref}} = 10$ μm at STP.
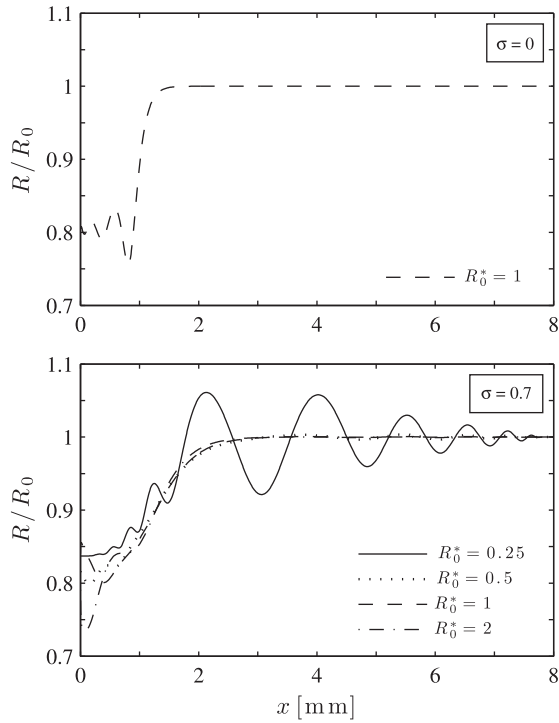
Fig. 11. Spatial evolution of the bubble radius with different equilibrium sizes for $\sigma = 0$ (top) and $\sigma = 0.7$ (bottom) at $t = 5.2$ μs for the unsteady shock propagation in Fig. 10.

profile in the averaged pressure seems unchanged during this period, and the shock propagation can thus be considered steady, regardless of unsteadiness associated with the individual bubble dynamics. In other words, the distribution yields an apparent

damping mechanism of the averaged shock dynamics. In this example, we can say that the effect of polydispersity dominates over the single-bubble-dynamic damping since the individual bubble dynamics have minor impact on the averaged shock structure. Because the bubbles with different sizes can oscillate with different phases, the phase cancellations in a polydisperse bubble cloud occur locally and the polydisperse cloud does not oscillate in volume. This collective effect thus leads to the smoothed shock structure.

4.4.2. Steady shock structure

The steady shock structures in the averaged liquid pressure are plotted in Fig. 13 with varying σ in the lognormal distribution (10). The position where the averaged pressure is $(p_{l0} + p_{lH})/2$ is set at $x = 0$. It transpires that the averaged shock structure becomes less oscillatory and the first peak become less steep as the distribution broadens. That is, the broader distribution can yield the more effective apparent damping, for the phase cancellation effect is emphasized with increasing σ. If the distribution is sufficiently broad ($\sigma = 0.7$), the shock profile in both averaged pressure and void fraction fields is practically monotonic; the polydisperse bubble cloud does not show oscillations in the void fraction due to the phase cancellations among the different-sized bubbles and can be regarded to behave quasistatically in spite of the individual bubble dynamics. Such a smoothed shock profile in a polydisperse mixture was experimentally identified by Beylich and Gülhan (1990).

Finally, we check the continuum model limitation. For the lognormal distribution (10), the mean bubble spacing is computed by

$$l = \left(\frac{3\alpha_0}{4\pi}\right)^{-\frac{1}{3}} \exp\left(\frac{3\sigma^2}{2}\right) R_0^{\text{ref}}. \tag{49}$$

For the case of $\alpha_0 = 0.005$ and $\sigma = 0.7$, we have $l \approx 20 R_0^{\text{ref}} = 0.2$ mm, which is much shorter than the wavelength of the smoothed shock profile; the scale separation constraint is adequately satisfied.
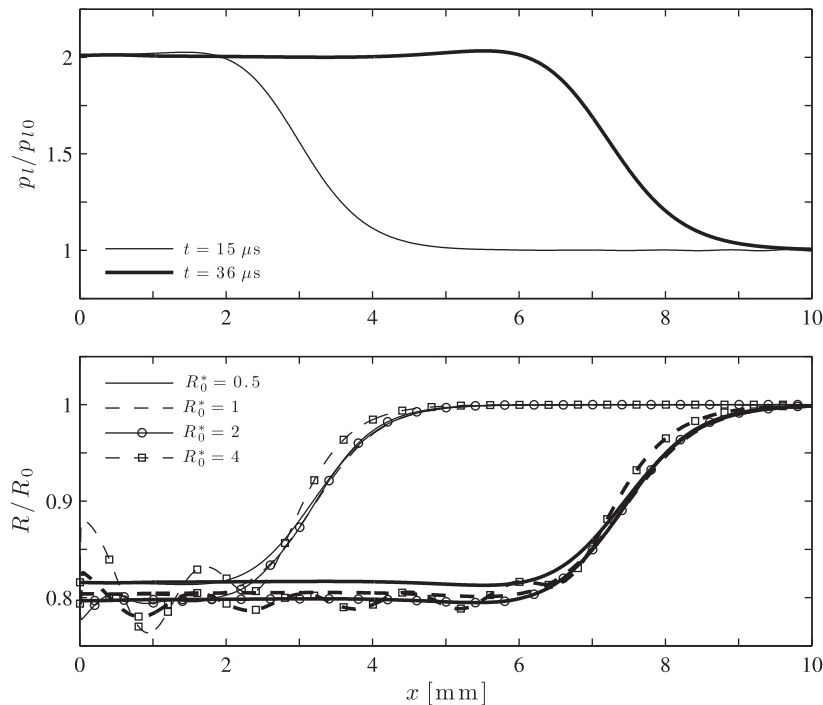

Fig. 12. Spatial evolution of the averaged liquid pressure (top) and the bubble radius with different equilibrium sizes (bottom) at two different times for the unsteady shock propagation. The thin and thick lines denote the solutions at $t = 15$ μs and 36 μs, respectively.
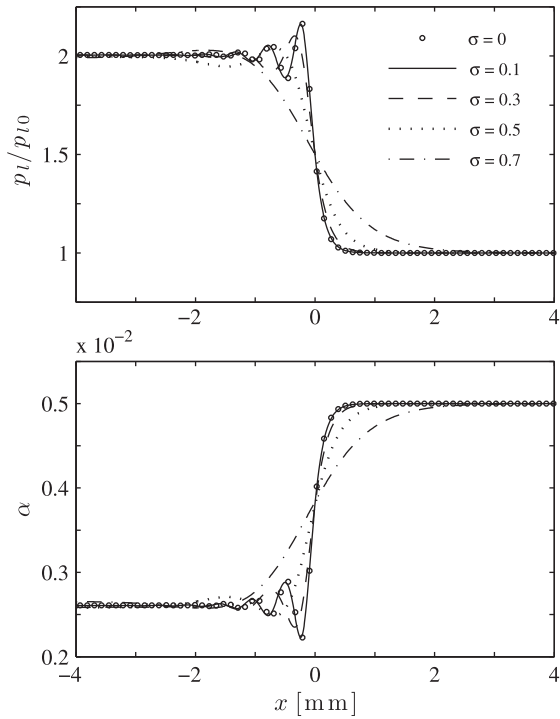
Fig. 13. Effect of the standard deviation, σ, in the lognormal bubble size distributions on the steady shock propagation.

4.5. Effect of the probable bubble size

We further conduct a parametric study of the probable bubble size, R_0^{ref}, and investigate its effect on the steady shock structures. In the example presented here, we also discuss the effect of poly-dispersity using the lognormal distribution (10) with $\sigma = 0$ and 0.7.

Fig. 14 shows the averaged liquid pressure distributions for steady shocks, with $p_{lH} = 2p_{l0}$, propagating in an air/water mixture of $\alpha_0 = 0.005$ at STP. We consider three probable bubble sizes $R_0^{\mathrm{ref}} = 5$ μm, 10 μm, and 20 μm. The spatial coordinate is normalized by R_0^{ref}. For the monodisperse cases, the first peak in the relaxation oscillations decreases with increasing R_0^{ref}; the bubble-dynamic damping depends on the bubble sizes and is critical to the averaged shock structures in the monodisperse mixture. However, the inclusion of the broad bubble size distribution leads to the fact that the shock profiles coincide in the normalized coordinate. Namely, the dynamics of the polydisperse bubble cloud are insensitive to the individual bubble dynamics, which are deemphasized by the apparent damping associated with the broad distribution.

4.6. Bubble screen problem

Bubble screens are a useful problem in understanding the fundamental physics of shock/bubble-cloud interactions and are used to prevent damage of submerged structures due to underwater explosions (Domenico, 1982). Reflection and transmission of linear wave propagation through a bubble screen were formulated by Carstensen and Foldy (1947) and Commander and Prosperetti (1989). Here, the interaction of a normal shock with a bubble screen is considered as an application example of the bubbly flow computations.

One-dimensional shock propagation through an air-bubble screen of $\alpha_0 = 0.005$ at STP in water is now computed with the initial void fraction distribution:

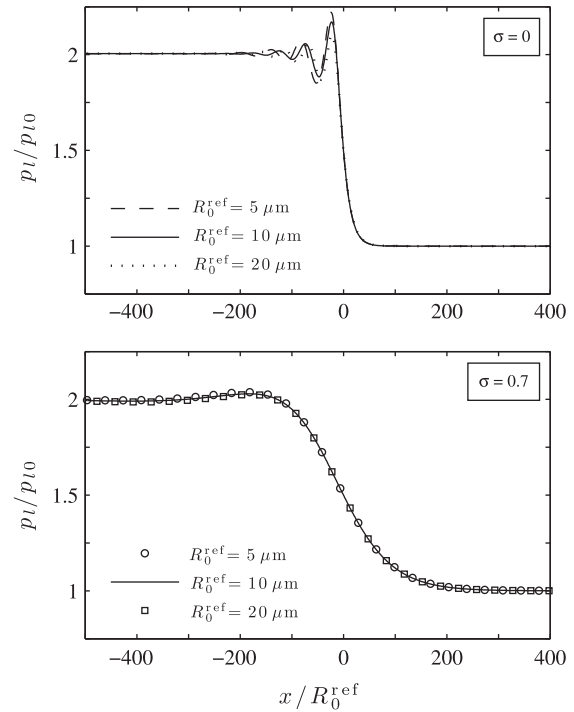$$\alpha = \begin{cases} \alpha_0, & \text{if } 0 < x < L, \\ \epsilon, & \text{otherwise,} \end{cases} \tag{50}$$

Fig. 14. Effect of the probable bubble size, R_0^{ref}, on steady shock propagation in an air/water mixture of $\alpha_0 = 0.005$ at STP. $M_s \approx 1.4$ for all the cases.
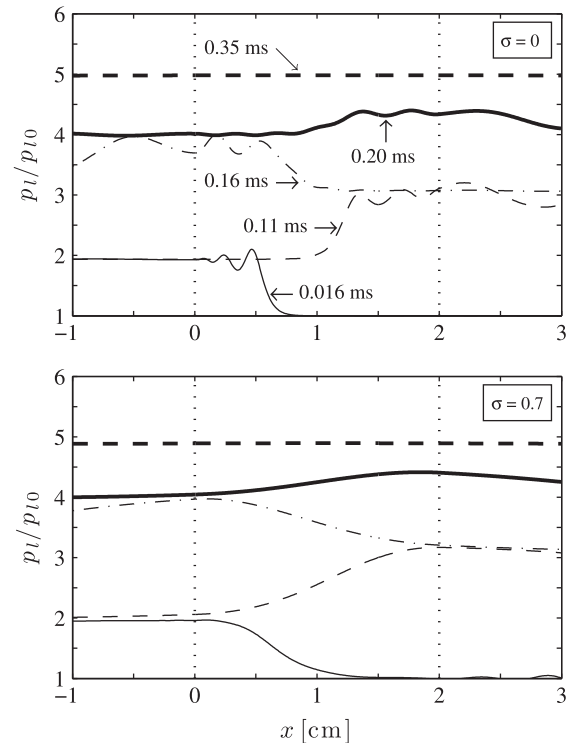

Fig. 15. Spatial evolution of the averaged liquid pressure for shock propagation through an air/water bubble screen of $\alpha_0 = 0.005$ and $R_0^{\mathrm{ref}} = 50$ μm. The screen is placed between the dotted lines.

where $0 < \epsilon \ll \alpha_0$ and $L = 2$ cm. The equilibrium bubble size in the screen ($0 < x < L$) is lognormally distributed about $R_0^{\mathrm{ref}} = 50$ μm and with $\sigma = 0$ and 0.7. The incident shock with $p_{lH} = 5p_{l0}$ is initially placed at $x < 0$.
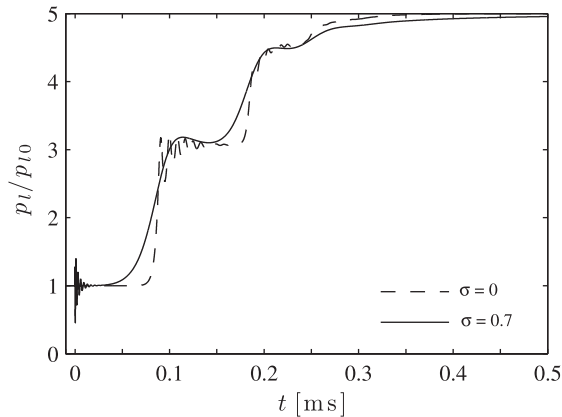
Fig. 16. Evolution of the liquid pressure for the transmitted waves in Fig. 14.

The snapshots of the averaged pressure distributions are shown in Fig. 15. At the left interface, the incident shock reflects as a rarefaction wave and transmits as a shock due to the fact that the acoustic impedance of the screen is smaller than that of water (i.e., $\rho c < \rho_l c_l$). The transmitted shock trapped in the screen keeps reflecting at the interfaces, and the pressure inside the screen eventually increases to the incident shock pressure. We see that the bubble size distribution smoothes out the oscillatory structure of the trapped waves.

The pressure just downstream of the screen is presented in Fig. 16. The precursory waves propagating with the sonic speed of water are measured at $t = 0$. Note that for the case with no bubble screen, the probe measurement would show an instantaneous jump to p_{lH} at $t \approx 0$. The transmitted shock waves leave the screen at late times, and the liquid pressure increases in a step-wise manner because of the reflections of the trapped waves in the screen. As expected, the distribution makes the averaged pressure evolution less oscillatory and broadens the averaged shock width. This implies that the polydisperse screen may be capable of more effectively cushioning impulsive loading than the monodisperse screen, but there is still a need to quantify the scattering effect in each realization in order to further investigate the practical implications.

5. Conclusions

The shock dynamics of bubbly flows with distributed bubble nuclei sizes have been explored based on the continuum approach. The contributions and findings of this paper can be summarized as follows.

The continuum bubbly flow equations incorporating a distribution of equilibrium bubble sizes were derived based on the ensemble-averaging technique. The single-bubble-dynamic model that includes the effects of thermal, viscous and acoustic damping was introduced to close the continuum model. It was confirmed that the volume averages will be equivalent to the ensemble averages if one appropriately chooses averaging volume under the scale separation constraint. One-way-coupled flow computations suggested that the different-sized bubbles oscillate with different frequencies and the phase cancellations can be regarded as an apparent damping of the mixture-averaged dynamics.

The fifth-order FV-WENO scheme with the HLLC Riemann solver was used to solve the continuum model. The computation of linear wave propagation in a bubbly liquid showed that the method is capable of accurately resolving wave dispersion, in a wide range of frequency, in continuum bubbly flows.

The numerical experiments of one-dimensional shock propagation in bubbly liquids showed that the averaged shock structure becomes less oscillatory as the bubble size distribution broadens. If the distribution is sufficiently broad, the shock profile is practically monotonic. Because the different-sized bubbles can oscillate with different frequencies, phase cancellations in a polydisperse mixture occur locally. For the broad distribution case, the polydisperse cloud does not oscillate in volume due to the phase cancellations and can be regarded to behave quasistatically, regardless of individual bubble dynamics. In this case, the effect of polydispersity dominates over the single-bubble-dynamic damping.

Appendix A. Computation of phase velocity and attenuation

Consider a wave of form, $\exp[j(2\pi ft - kx)]$, where j is the imaginary unit, f is the temporal frequency and k is the complex wave number ($=k_r - jk_i$). Following (Commander and Prosperetti, 1989), the phase velocity c^{ph} and attenuation a^{att} (in decibels per unit length) are defined as

$$c^{ph} = \frac{2\pi f}{k_r}, \quad a^{att} = 20(\log_{10} e)k_i. \tag{51}$$

The real and imaginary parts of the complex wave number can be determined based on the time history of the computed liquid pressure as follows. The evolution of the normalized pressure, $p' = (p_l - p_{l0})/(\epsilon p_{l0})$, is sampled at two different locations (say x_1 and x_2), and its discrete Fourier transform is then computed. The Fourier coefficients $\hat{p}'$ can be written as

$$\hat{p}'(x, f) = \hat{p}'_0 \exp[-k_i(f)x] \exp[-jk_r(f)x]. \tag{52}$$

Given the complex ratio $P_{1,2} = \hat{p}'(x_1, f)/\hat{p}'(x_2, f)$, the complex wave number is computed as

$$k_r = \frac{1}{\Delta x_{1,2}} \cos^{-1}[\Re\{P_{1,2}\}\exp(-\ln|P_{1,2}|)], \quad k_i = \frac{1}{\Delta x_{1,2}} \ln|P_{1,2}|, \tag{53}$$

where $\Delta x_{1,2} = x_2 - x_1$.

References

Ando, K., 2010. Effects of Polydispersity in Bubbly Flows. PhD Thesis, California Institute of Technology. <http://thesis.library.caltech.edu/5859/>.
Ando, K., Colonius, T., Brennen, C.E., 2009. Improvement of acoustic theory of ultrasonic waves in dilute bubbly liquids. J. Acoust. Soc. Am. 126, EL69–EL74.
Ando, K., Sanada, T., Inaba, K., Damazo, J.S., Shepherd, J.E., Colonius, T., Brennen, C.E., 2011. Shock propagation through a bubbly liquid in a deformable tube. J. Fluid Mech. 671, 339–363.
Balsara, D.S., Shu, C.-W., 2000. Monotonicity preserving weighted essentially non-oscillatory schemes with increasingly high order of accuracy. J. Comput. Phys. 160, 405–452.
Batchelor, G.K., 1970. The stress system in a suspension of force-free particles. J. Fluid Mech. 41, 545–570.
Batten, P., Clarke, N., Lambert, C., Causon, D.M., 1997. On the choice of wavespeeds for the HLLC Riemann solver. SIAM J. Sci. Comput. 18, 1553–1570.
Beylich, A.E., Gülhan, A., 1990. On the structure of nonlinear waves in liquids with gas bubbles. Phys. Fluids A 2, 1412–1428.
Biesheuvel, A., van Wijngaarden, L., 1984. Two-phase flow equations for a dilute dispersion of gas bubbles in liquid. J. Fluid Mech. 148, 301–318.
Bird, R.B., Stewart, W.E., Lightfoot, E.N., 1960. Transport Phenomena. Wiley.
Brennen, C.E., 1994. Hydrodynamics of Pumps. Oxford University Press.
Brennen, C.E., 1995. Cavitation and Bubble Dynamics. Oxford University Press.
Brennen, C.E., 2002. Fission of collapsing cavitation bubbles. J. Fluid Mech. 472, 153–166.
Brennen, C.E., 2005. Fundamentals of Multiphase Flow. Cambridge University Press.

Caflisch, R.E., Miksis, M.J., Papanicolaou, G.C., Ting, L., 1985a. Effective equations for wave propagation in bubbly liquids. J. Fluid Mech. 153, 259–273.

Caflisch, R.E., Miksis, M.J., Papanicolaou, G.C., Ting, L., 1985b. Wave propagation in bubbly liquids at finite volume fraction. J. Fluid Mech. 160, 1–14.

Campbell, I.J., Pitcher, A.S., 1958. Shock waves in a liquid containing gas bubbles. Proc. Roy. Soc. Lond. A 243, 534–545.

Carstensen, E.L., Foldy, L.L., 1947. Propagation of sound through a liquid containing bubbles. J. Acoust. Soc. Am. 19, 481–501.

Chahine, G.L., 1982. Cloud cavitation: theory. In: Proceedings of the Fourteenth ONR Symposium on Naval Hydrodynamics. pp. 165–194.

Cole, R.H., 1948. Underwater Explosions. Princeton University Press.

Colonius, T., d'Auria, F., Brennen, C.E., 2000. Acoustic saturation in bubbly cavitating flow adjacent to an oscillating wall. Phys. Fluids 12, 2752–2761.

Colonius, T., Hagmeijer, R., Ando, K., Brennen, C.E., 2008. Statistical equilibrium of bubble oscillations in dilute bubbly flows. Phys. Fluids 20, 040902.

Commander, K.W., Prosperetti, A., 1989. Linear pressure waves in bubbly liquids: comparison between theory and experiments. J. Acoust. Soc. Am. 85, 732–746.

d'Agostino, L., Brennen, C.E., 1989. Linearized dynamics of spherical bubble clouds. J. Fluid Mech. 199, 155–176.

d'Agostino, L., Brennen, C.E., Acosta, A.J., 1988. Linearized dynamics of two-dimensional bubbly and cavitating flows over slender surfaces. J. Fluid Mech. 192, 485–509.

Delale, C.F., Nas, S., Tryggvason, G., 2005. Direct numerical simulations of shock propagation in bubbly liquids. Phys. Fluids 17, 121705.

Delale, C.F., Tryggvason, G., 2008. Shock structure in bubbly liquids: comparison of direct numerical simulations and model equations. Shock Waves 17, 433–440.

Delale, C.F., Tunç, M., 2004. A bubble fission model for collapsing cavitation bubbles. Phys. Fluids 16, 4200–4203.

Domenico, S.N., 1982. Acoustic wave propagation in air-bubble curtains in water—Part I: history and theory. Geophysics 47, 345–353.

Einfeldt, B., Munz, C.D., Roe, P.L., Sjögreen, B., 1991. On Godunov-type methods near low densities. J. Comput. Phys. 92, 273–295.

Feuillade, C., 1996. The attenuation and dispersion of sound in water containing multiply interacting air bubbles. J. Acoust. Soc. Am. 99, 3412–3430.

Fujikawa, S., Akamatsu, T., 1980. Effects of the non-equilibrium condensation of vapour on the pressure wave produced by the collapse of a bubble in a liquid. J. Fluid Mech. 97, 481–512.

Gilmore, F.R., 1952. The Collapse and Growth of a Spherical Bubble in a Viscous Compressible Liquid. Hydrodynamics Laboratory Report 26-4, California Institute of Technology.

Kameda, M., Matsumoto, Y., 1996. Shock waves in a liquid containing small gas bubbles. Phys. Fluids 8, 322–335.

Kameda, M., Shimaura, N., Higashino, F., Matsumoto, Y., 1998. Shock waves in a uniform bubbly flow. Phys. Fluids 10, 2661–2668.

Katz, J., 1978. Determination of Solid Nuclei and Bubble Distributions in Water by Holography. Engineering and Applied Science Division Report 183-3, California Institute of Technology.

Kuznetsov, V.V., Nakoryakov, V.E., Pokusaev, B.G., Shreiber, I.R., 1978. Propagation of perturbations in a gas-liquid mixture. J. Fluid Mech. 85, 85–96.

LeVeque, R.J., 1992. Numerical Methods for Conservation Laws. Birkhäuser Verlag, Basel.

Lide, D.R. (Ed.), 2006. CRC Handbook of Chemistry and Physics, 87th ed. CRC Press (Chapter 6).

Liu, X.-D., Osher, S., Chan, T., 1994. Weighted essentially non-oscillatory schemes. J. Comput. Phys. 115, 200–212.

Nigmatulin, R.I., 1979. Spatial averaging in the mechanics of heterogeneous and dispersed systems. Int. J. Heat Mass Transfer 5, 353–385.

Nigmatulin, R.I., Khabeev, N.S., Hai, Z.N., 1988. Waves in liquids with vapour bubbles. J. Fluid Mech. 186, 85–117.

Nigmatulin, R.I., Khabeev, N.S., Nagiev, F.B., 1981. Dynamics, heat and mass transfer of vapour-gas bubbles in a liquid. Int. J. Heat Mass Transfer 24, 1033–1044.

Noordzij, L., van Wijngaarden, L., 1974. Relaxation effects, caused by relative motion, on shock waves in gas-bubble/liquid mixtures. J. Fluid Mech. 66, 115–143.

O'Hern, T.J., d'Agostino, L., Acosta, A.J., 1988. Comparison of holographic and Coulter counter measurements of cavitation nuclei in the ocean. J. Fluids Eng. 110, 200–207.

Omta, R., 1987. Oscillations of a cloud of bubbles of small and not so small amplitude. J. Acoust. Soc. Am. 82, 1018–1033.

Plesset, M.S., Prosperetti, A., 1977. Bubble dynamics and cavitation. Annu. Rev. Fluid Mech. 9, 145–185.

Preston, A.T., Colonius, T., Brennen, C.E., 2007. A reduced-order model of diffusive effects on the dynamics of bubbles. Phys. Fluids 19, 123302.

Prosperetti, A., 2001. Fundamental acoustic properties of bubbly liquids. In: Levy, M., Bass, H.E., Stern, R.R. (Eds.), Handbook of Elastic Properties of Solids, Liquids, and Gases, Elastic Properties of Fluids: Liquids and Gases, vol. 4. Academic, pp. 183–205.

Prosperetti, A., Crum, L.A., Commander, K.W., 1988. Nonlinear bubble dynamics. J. Acoust. Soc. Am. 83, 502–514.

Prosperetti, A., Lezzi, A., 1986. Bubbly dynamics in a compressible liquid (Part 1. First-order theory). J. Fluid Mech. 168, 457–478.

Qiu, J., Shu, C.-W., 2002. On the construction, comparison, and local characteristic decomposition for high-order central WENO schemes. J. Comput. Phys. 183, 187–209.

Roe, P.L., 1981. Approximate Riemann solvers, parameter vectors, and difference schemes. J. Comput. Phys. 43, 357–372.

Seo, J.H., Lele, S.K., Tryggvason, G., 2010. Investigation and modeling of bubble–bubble interaction effect in homogeneous bubbly flows. Phys. Fluids 22, 063302.

Shimada, M., Matsumoto, Y., Kobayashi, T., 2000. Influence of the nuclei size distribution on the collapsing behavior of the cloud cavitation. JSME Int. J., Ser. B 43, 380–385.

Shu, C.-W., Osher, S., 1988. Efficient implementation of essentially non-oscillatory shock-capturing schemes. J. Comput. Phys. 77, 439–471.

Takahira, H., 2004. A remark on the pressure terms in the Rayleigh–Plesset equation for cavitating flows. Trans. Jpn. Soc. Mech. Eng. B 70, 617–622.

Thompson, K.W., 1987. Time dependent boundary conditions for hyperbolic systems. J. Comput. Phys. 68, 1–24.

Thompson, P.A., 1972. Compressible-Fluid Dynamics. McGraw-Hill.

Toro, E.F., 1999. Riemann Solvers and Numerical Methods for Fluid Dynamics: A Practical Introduction, 2nd ed. Springer, New York.

Toro, E.F., Spruce, M., Speares, W., 1994. Restoration of the contact surface in the HLL-Riemann solver. Shock Waves 4, 25–34.

Tryggvason, G., Bunner, B., Esmaeeli, A., Juric, D., Al-Rawahi, N., Tauber, W., Han, J., Nas, S., Jan, Y.-J., 2001. A front-tracking method for the computations of multiphase flow. J. Comput. Phys. 169, 708–759.

van Wijngaarden, L., 1964. On the collective collapse of a large number of gas bubbles in water. In: Proceedings of the Eleventh International Congress on Applied Mechanics.

van Wijngaarden, L., 1968. On the equations of motion for mixtures of liquid and gas bubbles. J. Fluid Mech. 33, 465–474.

van Wijngaarden, L., 1972. One-dimensional flow of liquids containing small gas bubbles. Annu. Rev. Fluid Mech. 4, 369–396.

Wang, Y.-C., 1999. Effects of nuclei size distribution on the dynamics of a spherical cloud of cavitation bubbles. J. Fluids Eng. 121, 881–886.

Wang, Y.-C., Brennen, C.E., 1999. Numerical computation of shock waves in a spherical cloud of cavitation bubbles. J. Fluids Eng. 121, 872–880.

Watanabe, M., Prosperetti, A., 1994. Shock waves in dilute bubbly liquids. J. Fluid Mech. 274, 349–381.

Waterman, P.C., Truell, R., 1961. Multiple scattering of waves. J. Math. Phys. 2, 512–537.

Wylie, E.B., Streeter, V.L., 1993. Fluid Transients in Systems. Prentice Hall.

Zhang, Z.D., Prosperetti, A., 1994. Ensemble-averaged equations for bubbly flows. Phys. Fluids 6, 2956–2970.